Sensors and Actuators A 270 (2018) 252–261

Contents lists available at ScienceDirect

Sensors and Actuators A: Physical

journal homepage: www.elsevier.com/locate/sna

# Thin-film repulsive-force electrostatic actuators

Ethan W. Schaler[a], Tarek I. Zohdi[b], Ronald S. Fearing[a,*]

[a] Dept. of Electrical Engineering and Computer Sciences, University of California, Berkeley, CA 94720, USA
[b] Dept. of Mechanical Engineering, University of California, Berkeley, CA 94720, USA

ARTICLE INFO

*Article history:*
Received 11 August 2017
Received in revised form 6 December 2017
Accepted 21 December 2017
Available online 29 December 2017

*Keywords:*
Electrostatic actuator
Repulsive forces
Thin-films

ABSTRACT

We demonstrate thin-film repulsive-force electrostatic actuators that employ a new electrode pattern and are useful for low-force actuation applications. Compared to prior patterns, the new electrode geometry increases electrostatic force production by an order of magnitude (at equal voltages) and eliminates the most common shorting failure modes. These electrostatic actuators have stable open-loop operation with no pull-in instability, low mechanical hysteresis, and peak force in rest configurations. The actuators are fabricated with a planar, flex-circuit manufacturing process, allowing production at scale and over large areas. Two-layer out-of-plane linear actuators ($25 \times 10$ mm electrode area) were characterized: with 0–1000 V inputs ($40 \times 10^6$ V/m), blocked normal forces of 9.03 mN (36.1 Pa) were generated, and controllable linear displacements up to 511 μm were measured across an open loop bandwidth of 43 Hz. Finally, we present a 290 mg 1-DoF micro-mirror system for laser beam steering that employs a two-layer out-of-plane rotational actuator for open-loop stable operation with controlled angular displacements up to 5.1° at 1000 V/16 Hz.



## 1. Introduction

Advances in planar manufacturing have leveraged new processes and materials to develop a range of innovative robots and sensors [1–6]. Devices are composed of functional materials (films, fabrics, composites, inks, etc.) and use layering, patterning, folding, and bonding steps to form complex kinematic structures with integrated circuitry [3]. We apply these same standard manufacturing steps to fabricate thin-film repulsive-force electrostatic actuators.

Our initial goal is to produce cm-scale planar actuators, capable of generating mN forces and mm displacements at ∼30 Hz (video-compatible) frequencies, for applications in mobile robotics (i.e. a lightweight laser beam steering system) and beyond. Numerous viable actuator technologies exist at this scale: successful implementations of thermal/shape memory [7,8], piezoelectric [9], dielectric elastomer [10,11], and (attractive-force) electrostatic [12–15] planar actuators have all been demonstrated, and the merits of each have been comprehensively discussed [16,17]. Electrostatic actuators have the benefits of operating with larger displacements than piezoelectric actuators and higher speeds than thermal/shape memory actuators, and are well-suited for planar manufacturing. We focus specifically on repulsive-force electrostatic actuators, due to advantages in stability, controllability, and reliability over other electrostatic actuators.

In this paper, we demonstrate a new electrode geometry for planar repulsive-force electrostatic actuators (RFA) – see Fig. 1 – that operates with increased forces, displacements, and field strengths as compared to existing RFA designs. Our new RFA is simulated to establish performance bounds, fabricated using a flex-circuit planar manufacturing process, and characterized as the driving actuator in one degree-of-freedom linear and rotational systems.

## 2. Background

Electrostatic actuators typically consist of sets of moveable electrodes (conductive plates or combs) separated by an insulating dielectric, with electrostatic forces proportional to the charge accumulation on and electric fields between electrodes due to an applied electric potential. Operation of all electrostatic actuators is limited by electrical breakdown (shorting), which occurs when the electric field strength between electrodes exceeds the dielectric strength of the insulating medium ($3–110 \times 10^6$ V/m in air and $154–303 \times 10^6$ V/m in polyimide) [24–27]. A comparison of meso-scale electrostatic actuators is provided in Table 1.

At μm-scales, parallel plate actuators use electrodes arranged in pairs of parallel plates [28], and comb drive actuators use a pair of interdigitated combs [29]. To actuate, an applied volt-

* Corresponding author.
*E-mail address:* ronf@eecs.berkeley.edu (R.S. Fearing).
*URL:* http://robotics.eecs.berkeley.edu/ronf/ (R.S. Fearing).

https://doi.org/10.1016/j.sna.2017.12.054
0924-4247/

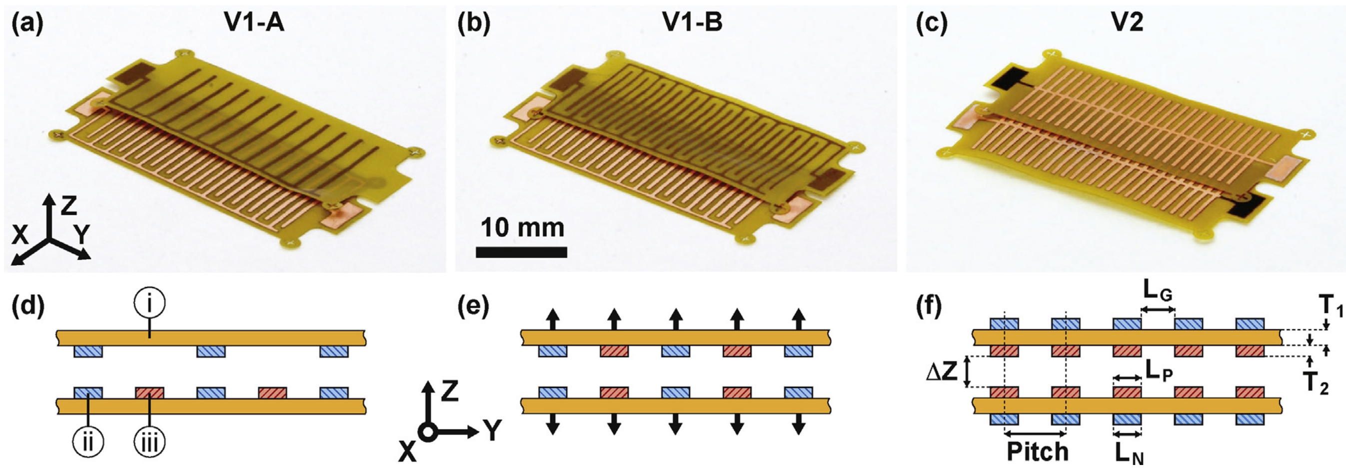


**Fig. 1.** Flexible, two-layer repulsive force actuator designs evaluated in this work: (a) V1-A, the electrode design used by S. He et al. [18], (b) V1-B, an improved design proposed by S. He et al. [19], (c) V2, the electrode design used in this work. For each actuator electrode design, the two functional layers are photographed (a–c) and the cross-sections are illustrated (d–f). Each actuator layer is composed of a polyimide substrate (i) with negative (ii) and positive (iii) electrodes. Actuator layers experience a net repulsive electrostatic pressure, illustrated in (e). Actuator dimensions include the substrate ($T_1$ = 25 μm) and electrode ($T_2$ = 18 μm) thickness, positive ($L_P$ = 500 μm) and negative ($L_N$ = 500 μm) electrode width, gap between adjacent electrodes ($L_G$ = 500 μm), and inter-layer height ($\Delta Z$).

age draws the electrodes together for gap-closing operation. To improve stroke length, the actuator output is often coupled to an inchworm mechanism [21]. At mm-scales, integrated force arrays [22,30] and distributed electrostatic actuators [12] are massively-parallelized actuators with 100s–1000s of connected parallel plate electrode units. Actuators at this scale are micro-fabricated, have high force density, low strains, and the highly-parallelized designs have low yields [30].

At cm-scales, dielectric elastomer actuators (DEA) use compliant electrodes fabricated on each side of low modulus elastomer film [20,31,32]. DEAs generate large strains (60%) and high pressures (100s kPa) during operation: applied voltages thin the elastomer (distance between the electrodes) and stretch the cross-sectional area. DEAs also exhibit significant viscoelastic behavior due to the compliant elastomer film. Gap-closing distributed electrostatic actuators [12], stacked electrostatic actuators [13], and zipper electrostatic actuators [14] generate mm to cm strokes, sub-N forces, and 100s Pa pressures. Linear surface-drive electrostatic film actuators [23] and motors [33] are flex-circuit devices that generate up to 4.4 N forces and 100s Pa pressures.

Repulsive force electrostatic actuators (RFA) are a subset of electrostatic actuators that generate a net repulsive force (instead of attractive force) through clever configuration of the 2+ sets of differentially polarized electrodes [33]. Similarly charged electrodes oppose one another on moveable layers to generate the inter-layer repulsive force. Oppositely charged electrodes establish the electric fields and potential gradients in the actuator, but minimize attractive forces between moveable layers by: spacing oppositely-charged electrodes further apart than like-charged electrodes to produce weaker out-of-plane attractive forces, using symmetry to minimize in-plane attractive forces, and having attractive forces act as internal body forces on noncompliant substrates.

RFAs in general have low complexity, generate peak force at the initial displacement, have linear or rotational outputs based on suspension design (minimizing transmission requirements), and avoid many common failure modes of electrostatic actuators – RFAs have no pull-in limit, no increased likelihood of breakdown as electrodes displace normally, and no stiction problem.

RFAs were first reported by W. Tang et al. [33]: electrodes patterned below a comb drive linear lateral resonator were used as

**Table. 1**
Survey of meso-scale electrostatic actuators, with key normalized metrics highlighted in grey.

| Design | A / mm x mm | L / mm | ΔL / mm | ε / % | E / V/m | F / N | F/A / N/m² | BW / Hz | Source |
|---|---|---|---|---|---|---|---|---|---|
| Dielectric Elastomer | 0.070 x 18 | 21 | – | +61* | $43 \cdot 10^{6}$* | 0.75 | $600 \cdot 10^{3}$ | 15 | [20] |
| Parallel Plate Inchworm | 0.040 x 1.56 | 0.97 | 0.124 | +13 | $21 \cdot 10^{6}$ | $2.23 \cdot 10^{-3}$ | $1.38 \cdot 10^{3}$ | 39* | [21] |
| Integrated Force Array | 0.002 x 1 | 10 | 0.700 | -7.0 | $80 \cdot 10^{6}$ | $62 \cdot 10^{-6}$ | $28 \cdot 10^{3}$ | – | [22] |
| Stacked Electrostatic | 54 x 54 | 2.27 | 0.420 | -20.5 | $28 \cdot 10^{6}$ | 1.27 | 435 | – | [13] |
| Electrostatic Film Slider | 50 x 100 | 0.380 | – | – | $14.3 \cdot 10^{6}$ | 4.4 | 880 | – | [23] |
| Distributed Electrostatic | 0.005 x 4 | 5 | 0.028 | -0.6 | $33 \cdot 10^{6}$ | $6.3 \cdot 10^{-6}$ | 315 | 1.6* | [12] |
| Distributed Electrostatic | 31 x 28 | 11 | 4 | -36 | $5 \cdot 10^{6}$ | – | – | – | [12] |
| Zipper Electrostatic | 50 x 10 | 18.1 | 18 | -99* | $110 \cdot 10^{6}$ | – | – | 12 | [14] |
| Repulsive Force | 3.26 x 3.26 | 0.004 | 0.086 | +2000 | $3.8 \cdot 10^{6}$ | $5 \cdot 10^{-6}$* | 2.9* | 80-200 | [18] |
| **V1-A** | 80 x 10 | 0.136 | – | – | $2 \cdot 10^{6}$ | $2.74 \cdot 10^{-3}$ | 3.4 | – | This Work |
| **V1-B** | 25 x 10 | 0.136 | – | – | $2 \cdot 10^{6}$ | $1.04 \cdot 10^{-3}$ | 4.2 | – | |
| **V2** | 25 x 10 | 0.431 | 0.511 | **+119** | $40 \cdot 10^{6}$ | $9.03 \cdot 10^{-3}$ | **36.1** | **43** | |

*A* – area (orthogonal to stroke axis); *L* – length (parallel to stroke axis); *E* – electric field strength; Δ*L* – stroke length; ε – strain (Δ*L*/*L*, with + indicating expansion); *F* – force; *F*/*A* – area force density; BW – frequency bandwidth. (*) denotes properties calculated from provided information.

a tunable electrostatic spring to control the height of the combs translating over the substrate, with measured out-of-plane displacements of 0.4–2 μm (from an initial 2 μm offset) at 30 V [34]. RFAs were further developed as a MEMS actuator for controllable 1-DoF [19,35–37] and 3-DoF [18,38] micro-mirrors. Modeling of two- and three-layer actuators and optimization of the electrode geometry show that maximum force is achieved when electrodes have equal width and spacing ($L_G = L_P = L_N$), and maximum out-of-plane displacement is proportional to in-plane electrode pitch [35,36]. Multiple RFAs were successfully fabricated with PolyMUMPs, including a 3-DoF micro-mirror system capable of out-of-plane translation (86 μm) and roll/pitch rotation (±1.5°) at 200 V [18].

We successfully scale up these RFAs for operation at the meso-scale. The V1 designs (Fig. 1d and e) employ the same electrode configurations as prior works: alternating positive- and negative-voltage electrodes on one side of a shared substrate, with multiple layers aligning similarly-polarized electrodes on the common side. The new V2 design (Fig. 1f) reconfigures the electrodes: rows of positive- and negative-voltage electrodes are aligned on opposite sides of a shared substrate, with multiple layers aligning similarly-polarized electrodes on the common side. In V1, maximal electric fields are directed between adjacent electrodes, so peak voltage, field, and force are all limited by the dielectric strength of air, the inter-electrode spacing ($L_G$), and any layer misalignment ($\Delta Y$). In V2, maximal electric fields are directed through the substrate, so these properties are independent of electrode geometry or layer alignment, and limited only by the dielectric strength of the substrate. Relatedly, the principle failure modes in V1 are shorting between adjacent electrodes (due to manufacturing defects) or layers (due to layer misalignment during set-up or operation) – problematic in dynamic systems; in V2, shorting is only possible through the more resilient substrate.

## 3. Simulation & results

We developed a 2D numerical simulation of the RFA in MATLAB. The actuator electrostatics (charge distribution, electric potential, and forces) are solved using an explicit finite differences method, with a high-fidelity, non-uniform rectangular mesh and iterated to convergence.

### 3.1. Modeling

Analytical models for two-layer RFA systems were derived by S. He et al. [19,36], using conformal transformations to map unit cells of the RFA electrode configuration into a parallel plate electrode configuration for ease of calculation. This transformation, however, assumes unit cells with perfectly aligned, symmetric electrodes – two design requirements not guaranteed when designing these actuators for manufacturing. Agreement between analytical models and numerical simulations has been verified [19], thus only numerical simulations are used in this paper.

The constitutive equations at each node ($\underline{x}_i$) of the simulation, relating electric potential ($V$), electric field ($\underline{E}$), displacement field ($\underline{D}$), and polarization density ($\underline{P}$), are defined as:

$$\underline{E} = -\nabla V \tag{1}$$

$$\underline{D} = \varepsilon_r \varepsilon_0 \underline{E} = \varepsilon_0 \underline{E} + \underline{P} \tag{2}$$

$$\underline{P} = (\varepsilon - \varepsilon_0)\underline{E}, \quad \text{with}\ \varepsilon = \varepsilon_r \varepsilon_0 \tag{3}$$

Net charge density ($\rho$) in the system consists of bound ($\rho_b$) and free ($\rho_f$) charge densities, related by:

$$\rho = \rho_f + \rho_b \tag{4}$$

$$\rho_f = \nabla \cdot \underline{D} \tag{5}$$

$$\rho_b = -\nabla \cdot \underline{P} \tag{6}$$

Combining (1), (2) and (5), and applying partial differentials:

$$\nabla \cdot \varepsilon \nabla V = -\rho_f \tag{7}$$

$$\varepsilon_y V_y + \varepsilon V_{yy} + \varepsilon_z V_z + \varepsilon V_{zz} = -\rho_f \tag{8}$$

The partial derivatives have a finite differences formulation (2nd order, using Lagrangian polynomials for non-uniform grid interpolation) [39] centered at $\underline{x}_i$ of:

$$\begin{aligned} \varepsilon_y &= a_{y,i}\varepsilon(\underline{x}_{i-1}) + b_{y,i}\varepsilon(\underline{x}_i) + c_{y,i}\varepsilon(\underline{x}_{i+1}) \\ V_y &= a_{y,i}V(\underline{x}_{i-1}) + b_{y,i}V(\underline{x}_i) + c_{y,i}V(\underline{x}_{i+1}) \\ V_{yy} &= a_{yy,i}V(\underline{x}_{i-1}) + b_{yy,i}V(\underline{x}_i) + c_{yy,i}V(\underline{x}_{i+1}) \end{aligned} \tag{9}$$

with $a_i$, $b_i$, $c_i$ defined in [39]. Dirichlet boundary conditions at the electrodes – $V_- = 0$ and $V_+ = V_{Applied}$ – mimic the voltage source powering the actuator. Neumann boundary conditions are defined along the system perimeter – $\partial V / \partial \underline{n} = 0$. Boundaries of the simulation space are at least 5 times the dimensions of the actuator-containing space, to mitigate computation artifacts due to the finite boundaries. Meshing of the simulation space uses a non-uniform rectangular mesh, with highest mesh density at electrode and substrate surfaces to capture the electric fringing field behavior (Fig. A.1).

The voltage distribution in this system is calculated by solving for $V(\underline{x}_i)$ in (8) and (9) (assuming $\rho_f = 0$ outside electrodes), reimposing boundary conditions, and iterating to convergence. Once V converges, $\underline{E}$, $\underline{P}$, and $\rho$ can be calculated directly.

The electrostatic force on a region of the actuator is:

$$\underline{F} = \iiint_{\mathbb{V}_\mathbb{E}} (\rho_f \underline{E}) d\mathbb{V} + \iiint_{\mathbb{V}_\mathbb{D}} (\rho_b \underline{E}) d\mathbb{V} + \iint_{\mathbb{S}} \left(\frac{1}{2}(\sigma_f + \sigma_b)\underline{E} \cdot \hat{n}\right) d\mathbb{S} \tag{10}$$

with force contributions from the electrode ($\mathbb{V}_\mathbb{E}$) and dielectric ($\mathbb{V}_\mathbb{D}$) volume interiors and the interfacing surfaces between these regions ($\mathbb{S}$), and with corresponding free ($\sigma_f$) and bound ($\sigma_b$) surface charge densities. To accurately quantify the net repulsive force between layers – which is roughly 2-orders of magnitude smaller than the attractive body forces between electrodes on each side of a dielectric substrate – the simulation is assumed to converge when forces on each electrode change by less than 0.05% over 500 iterations.

### 3.2. Simulation results

The simulation results presented in Fig. 2 demonstrate that meso-scale actuators (2.5 cm$^2$ area with 500 μm electrode widths and gaps) can generate mN-range forces with >500 μm gaps at 1 kV potentials. The electric potential distributions for the three actuator designs are shown in Fig. 2a-c.

From Fig. 2e, the V1 designs have a maximum electric field strength limited by the air dielectric to $5.0 \times 10^6$ V/m (for $L_G$ = 500 μm) and a corresponding maximum voltage of 2.5 kV [24]. The V2 design uses a polyimide substrate instead of air as the insulating dielectric between oppositely-polarized electrodes, which increases the maximum electric field strength to $236 \times 10^6$ V/m (47× increase) and maximum voltage to 5.9 kV (2.3× increase). Note that in the V2 design, the field strength in air around the electrodes can exceed the dielectric strength of air – indeed, fields above $5.0 \times 10^6$ V/m extend approximately 50 μm from the edges of electrodes at 1000 V. This can cause localized air ionization – without

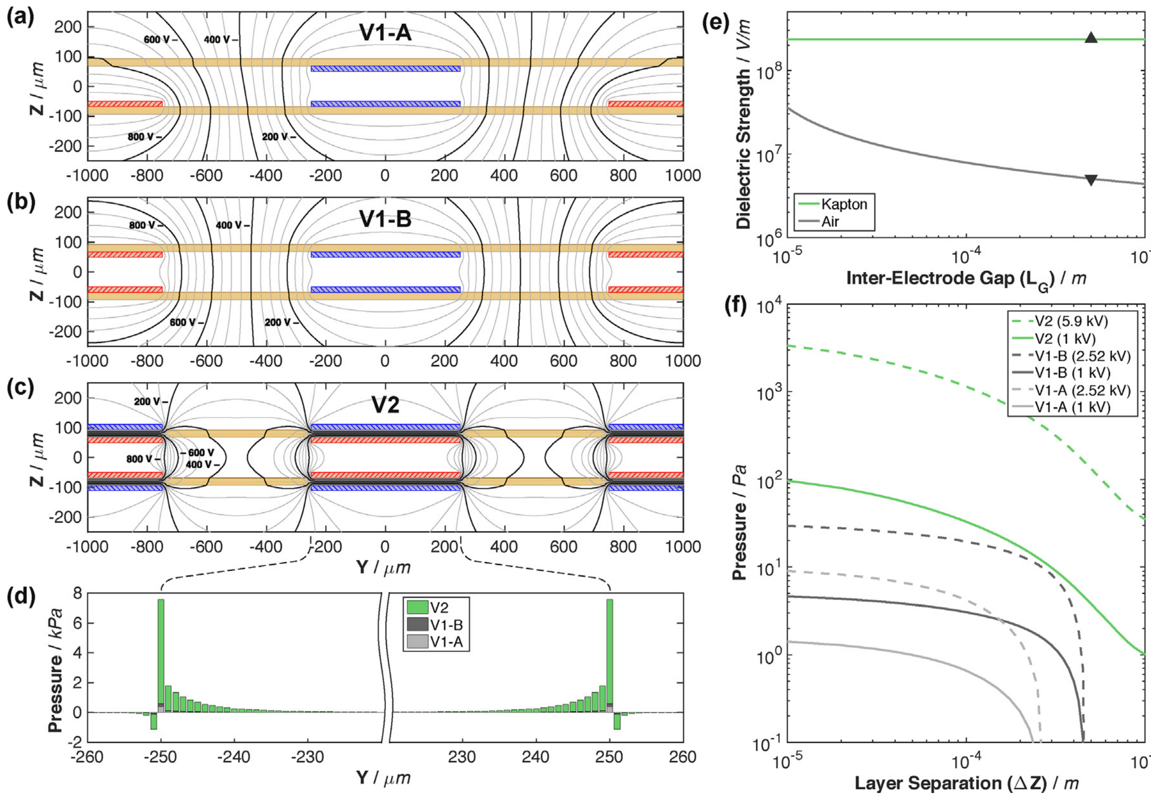


**Fig. 2.** Simulation results for the repulsive-force electrostatic actuator. Electrostatic potential ($V$) for designs V1-A (a), V1-B (b), and V2 (c), with electrodes operating at 0 V (blue)/1000 V (red) and dielectric substrate (orange). (d) Net electrostatic pressure across the top layer of each design, focusing on the center electrode and with 1 μm mesh size. (e) Dielectric strength at breakdown versus inter-electrode gap ($L_G$) in polyimide [26,27] and air [24,25]. Manufactured V1-A/B actuators (with $L_G$ = 500 μm) are limited by air breakdown at $5.0 \times 10^6$ V/m (▼); V2 actuators are limited by polyimide breakdown at $2.4 \times 10^8$ V/m (▲). Note that in V2 actuators, the field strength around the electrodes can exceed the dielectric strength of air without breakdown, as all shorting paths between positive/negative electrodes must pass through the more robust polyimide substrate. (f) Net electrostatic pressure produced by a complete actuator versus layer separation ($\Delta Z$) in each design. Operating voltage (in legend) is either 1 kV or maximum voltage corresponding to predicted electrostatic breakdown field strength from (e). (For interpretation of the references to color in this figure legend, the reader is referred to the web version of the article.)

breakdown – as all shorting paths between positive/negative electrodes must still pass through the more robust polyimide substrate.

From Fig. 2f, the new V2 electrode design generates consistently greater electrostatic pressures and forces than comparable V1-A/B designs. For actuators with equivalent configurations ($L_G$, $L_P$, $L_N$ = 500 μm, $H$ = 50 μm, 2.5 cm$^2$ actuator area) and operating at $V$ = 1 kV, V2 produces estimated forces of 13.1 mN, compared to 0.934 mN for V1-B (14× decrease) and 0.249 mN for V1-A (53× decrease). Operating at their respective breakdown voltages, V2 generates forces of 455 mN, compared to 5.95 mN for V1-B (76× decrease) and 1.59 mN for V1-A (286× decrease). Interestingly, above certain inter-layer heights, V1-A and V1-B actuators transition to a net attractive force between layers, while V2 does not exhibit this behavior and always produces a net repulsive force. Finally, the significance of the fringing fields is highlighted in Fig. 2d, where 90% of the actuator's force is generated by the 20 μm of electrode area nearest each edge – 4% of total actuator area. Future fabricated actuators can thus generate greater electrostatic pressure via increasing electrode density (reduced electrode width ($L_P$, $L_N$) and pitch) up to manufacturing limits.

## 4. Fabrication

A flex-circuit manufacturing process is used to produce planar repulsive-force electrostatic actuators patterned with the V1-A/B and V2 electrode designs introduced in Section 3. The fabrication process is illustrated in Fig. A.2; fabricated actuator layers are shown in Fig. 1 and a magnified view of V2 is provided in Fig. 3.

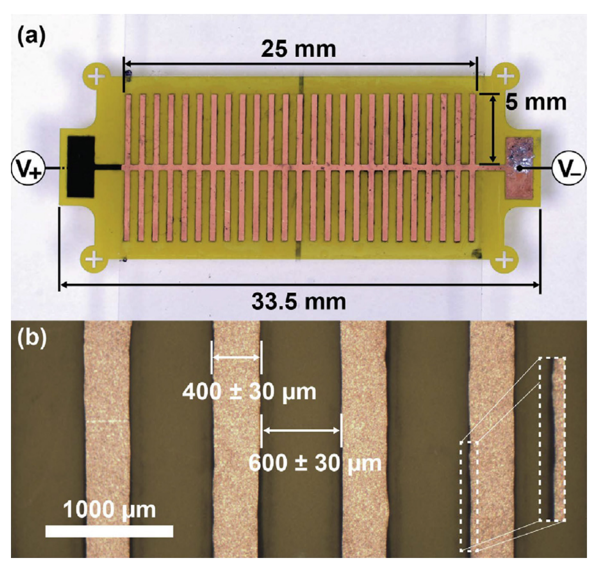


**Fig. 3.** Photo of fabricated two-sided, design V2 actuator layer (a), with magnified view of electrodes (b). Dashed region highlights minor variation between widths of front-side (copper) and back-side (dark region) electrodes; over-etching results in $L_P$, $L_N$ ≈ 400 μm. Also note visual alignment marks (+) at actuator corners.

### 4.1. Design

RFA layers are fabricated out of Pyralux (DuPont, AP 8515E) – a double-sided laminate composed of copper foil (18 μm) electrodeposited on a polyimide substrate (25 μm) that is designed for high-voltage and flex-circuit applications.

The polyimide substrate provides resilience to electrical breakdown (236 V/μm dielectric strength at 25 μm thick), operation up to 6 kV, low dielectric losses (dissipation factor under 0.003), trivial mechanical creep at sub-MPa loading, and high folding endurance (285,000 cycles) [26], although time-to-failure decreases with faster charging/discharging rates and higher peak-to-peak voltages [40,41]. The Cu foil is ductile, has good flexural endurance (>6000 cycles), and is resistant to delamination (1.6 N/mm peel strength) [27]. Thus, the actuators are mechanically resilient to the physical impulses (drops, collisions, etc.) that would be common during use in a mobile robot platform.

### 4.2. Process

Actuator layers are fabricated using a positive wet etching process, shown in Fig. A.2. Device layers are fabricated from Pyralux (DuPont, Pyralux AP 8515E), and mask layers consist of polyimide sheets (American Durafilm, Kapton 100HN (25 μm)) with thermal adhesive (GBC, Octavia Hot Mount Adhesive) laminated onto one side. Mask layers are secured to both sides of a device layer. The actuator electrode pattern is cut into the mask layers (positive mask) and the actuator substrate extents are cut through all mask/device layers using a UV laser cutter (PhotoMachining Inc., 355 nm). Excess mask and substrate material are removed manually. The mask/device layers are run through a laminator to set the thermal adhesive and provide an etch barrier. Any exposed thermal adhesive is removed with acetone (Fischer Scientific). The device layer is selectively etched with ferric chloride (MG Chemicals, $FeCl_3$) to pattern the Cu electrodes. Mask layers are released with acetone and the device layer is cleaned with water. Production time is approximately 4 hours per sheet of actuator layers.

Final assembly of the actuator layers can be performed multiple ways: laminating the layers to substrates (Section 5.1), attaching the layers to a flexible suspension (Section 5.2), or folding preconnected layers over one another (Section 6). In each instance, power wires are directly soldered to electrode pads on each layer, and visual alignment marks (+) at the actuator corners are used to ensure precise alignment between layers.

### 4.3. Process advantages

From a manufacturing perspective, this thin-film process enables cheaper fabrication of actuator layers with greater surface area, and provides significant design freedoms over conventional MEMS processes. The fabrication uses 2–3 patterning steps and 1 etch step to fabricate batches of complete V1 or V2 actuator layers. Actuators with +2 layers can be assembled by stacking discrete layers or folding up a sheet of connected units. Within each layer, the substrate provides all necessary mechanical structure and electrical insulation for the positive/negative voltage traces (no extra laminates required). For each device, interface leads can be directly soldered to electrodes without compromising the substrate (no wire-bonder needed). MEMS processes, in comparison, require numerous deposition, masking, and etching steps to produce a single spring-suspended device layer with routing for positive/negative lines on a floating dielectric. As a result, the V1-A design is simple to produce with PolyMUMPS, while the V1-B design is more complex and our new V2 design is entirely incompatible.

## 5. Characterization & results

### 5.1. Force measurements

Blocked force measurements of the RFAs were performed using the experimental set-up shown in Fig. 4. Alignment sensitivity of the actuator layers is measured by translating the two layers relative to one another in discrete *X*-, *Y*-, and *Z*-axis offsets ($\Delta X$, $\Delta Y$, $\Delta Z$), as shown in Fig. 5.

#### 5.1.1. Experimental

Two actuator layers are laminated to individual glass microscope slides (Fischer Scientific, 75 × 25 × 1 mm) with thermal adhesive. One glass slide is mounted on a stack of two linear stages (Newport, 423 Series) to provide *X*-/*Y*-axis offsets, with the actuator

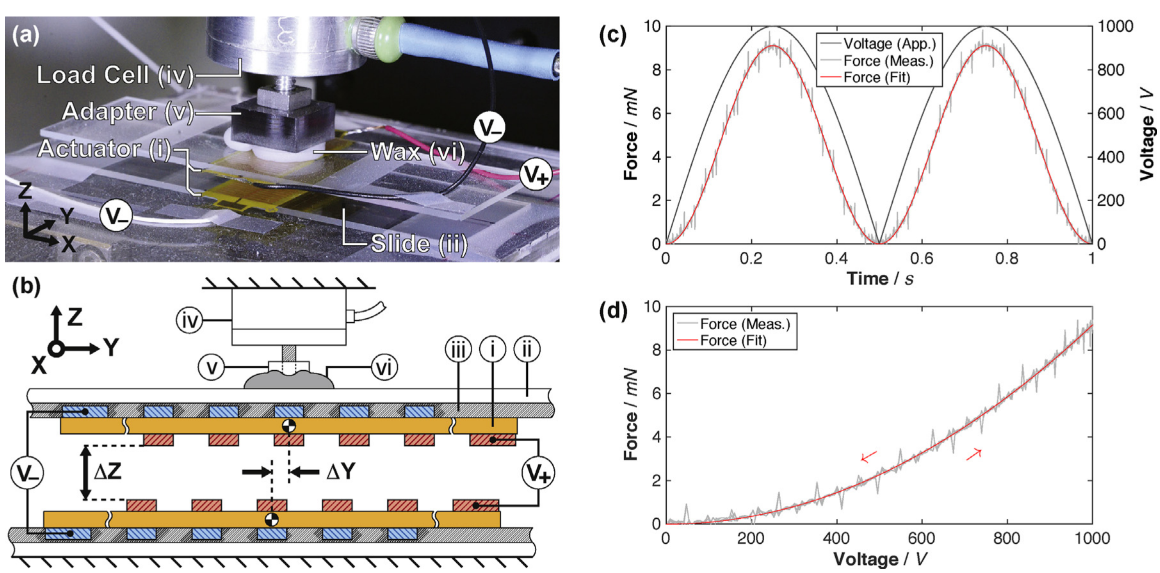


**Fig. 4.** Testing setup for blocked force characterization (a) with mechanical diagram (b) (electrical diagram in Fig. A.3). Two actuator layers (i) are bonded to glass slides (ii) with thermal adhesive (iii). The bottom layer sits on a multi-DoF stage; the top layer connects to a load cell (iv) via an adapter (v) and wax (vi), and is aligned parallel to the bottom layer. (c and d) Force characterization at $\Delta X$, $\Delta Y$ = 0 μm and $\Delta Z$ = 50 μm. Applied voltage is the square-root of a sinusoid at 2 Hz and 1000 V peak-to-peak. (c) Force (measured and sinusoidal fit) and applied voltage versus time; (d) force (measured and quadratic fit) versus voltage. Force data is unfiltered, and periodic peaks are 60 Hz noise.

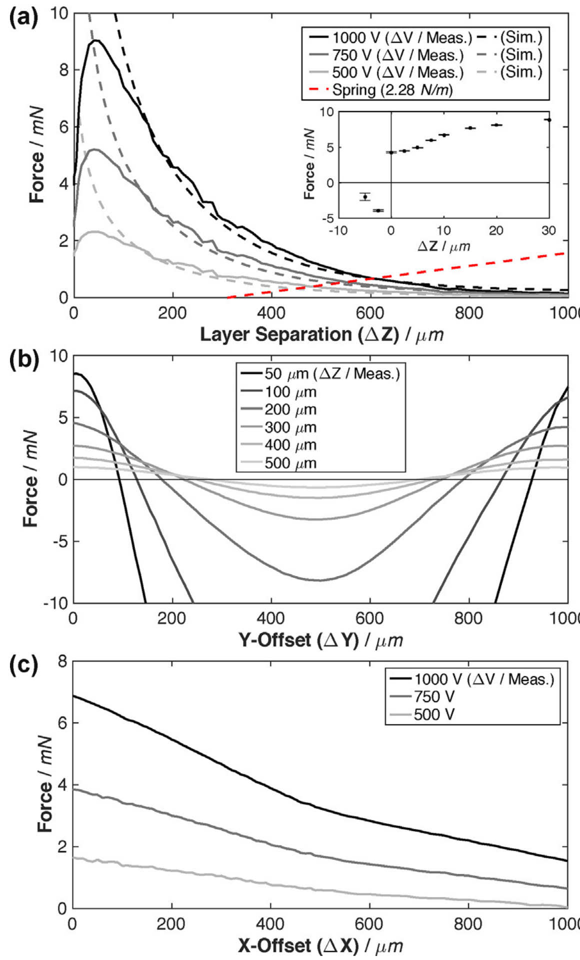


**Fig. 5.** Repulsive normal force characterization for the V2 actuator at a range of $\Delta X$, $\Delta Y$, and $\Delta Z$ offsets, with square-root of sinusoid inputs at 2 Hz/1000 V peak-to-peak. (a) Measured (Meas.) and simulated (Sim.) force versus $\Delta Z$ ($\Delta X$, $\Delta Y = 0\,\mu m$, $\bar{\sigma} = 0.042$ mN) at three voltages, and suspension spring force ($k_S = 2.28$ N/m). Inset figure shows near-/in-contact behavior, with mechanical contact force removed. (b) Force versus $Y$-axis offsets ($\Delta Z = 50$–$500\,\mu m$, $\Delta X = 0\,\mu m$, $\bar{\sigma} = 0.127$ mN). (c) Force versus $X$-axis offsets ($\Delta Z = 100\,\mu m$, $\Delta Y = 0\,\mu m$, $\bar{\sigma} = 0.045$ mN).

layer face-up. A single-axis load cell (Omega, LCFA-50G) is mounted to a third linear stage providing $Z$-axis offsets, suspended over the other stages, and an interface block is secured to the end of the load cell input shaft. The second glass slide, with actuator face-down, is placed and aligned on top of the first actuator layer. Liquid paraffin wax is poured on the top side of the glass slide, and the load cell with interface block is lowered into the liquid wax and allowed to solidify. The wax provides mechanical connection between the actuator and load cell while guaranteeing the two actuator layers are parallel. The top actuator layer can then be raised away from the bottom layer.

A LabView interface controls the experiment (Fig. A.3). A low-voltage drive signal ($V_{Drive}$) – in this case a 2 Hz, 0–10 V square-root of sinusoid waveform – is generated by a DAQ (National Instruments, NI USB 6341) and supplied to a high-voltage amplifier (Trek, PZD700 Piezo Driver/Amplifier). The amplifier provides 100× gain to $V_{Drive}$, and this signal then powers the actuator. Voltage ($V_{VP}$) and Current ($V_{CP}$) probes provide measurement of the actuator's electrical properties during testing. The load cell – a full Wheatstone bridge strain gauge circuit – measures the electrostatic normal force applied to the top actuator layer and a strain gauge amplifier (Techkor Instrumentation, MEPTS-9000) boosts this signal ($V_{Sense}$) by 100×. $V_{Sense}$ is then logged by the DAQ.

### 5.1.2. Results

Maximum repulsive force (9.03 mN) is generated by a two-layer V2 actuator in a ($\Delta X$, $\Delta Y = 0\,\mu m$, $\Delta Z = 50\,\mu m$) configuration at 1000 V. Recorded actuator behavior in this configuration is provided in Fig. 4c and d, and shows the quadratic relationship between the applied voltage and blocked force. Operation of a well-aligned (in the $X$/$Y$-plane) actuator will apply purely normal ($Z$-axis) force to the top layer. Repulsive force increases with the inverse square of $Z$-axis offsets (Fig. 5a), to a maximum of 9.03 mN (at $\Delta Z = 50\,\mu m$), and has good agreement with the simulated forces. Closer than this ($\Delta Z < 50\,\mu m$), electrode imperfections produce non-uniformities in the electric field that reduce the repulsive force. Upon contact ($\Delta Z = 0\,\mu m$), the internal ($V_+$) electrodes act as a single conductive body, which redistributes the surface charge and generates a net attractive force between the actuator layers (Fig. 5a, Inset).

$Y$-axis offsets (Fig. 5b, $\Delta Y > 0\,\mu m$) between the layers reduce the repulsive normal force, and sufficient lateral offsets can actually transition the net repulsive force to an attractive force. The $\Delta Y$ transition from repulsive to attractive force varies with $\Delta Z$ : $\Delta Y_{Trans.} = 92$, 128, 178, 275 μm (9.2–27.5% phase offset, given the 1 mm pitch electrodes) for $\Delta Z = 50$, 100, 200, 500 μm, respectively, so closely spaced layers tolerate less $\Delta Y$ misalignment. Maximum attractive force occurs at $\Delta Y = 500\,\mu m$ (50% phase offset) and maximum repulsive force occurs at 0%/100% phase offsets. A $Y$-axis shear force is also produced during the transition from pure repulsive to pure attractive modes. This behavior demonstrates the need to assemble RFAs with precise lateral alignment to ensure maximum repulsive forces are generated (and attractive forces are avoided).

$X$-axis offsets (Fig. 5c, $\Delta X > 0\,\mu m$) reduce the overlap between electrode traces on each layer and proportionally reduce the repulsive normal force. The slope changes at $\Delta X = 500\,\mu m$ when the centerline trace no longer overlaps (see Fig. 3). Electrode traces remain well-aligned with respect to the $Y$-axis, avoiding a transition from repulsive to attractive force.

## 5.2. Displacement measurements

Free displacement measurements of the RFAs were performed using the set-up shown in Fig. 6, with results in Fig. 7. The actuator top layer is suspended on a parallel 4-bar suspension (Fig. A.4) that provides orientation, $Z$-axis compliance for large displacements, and $X$-/$Y$-axis stiffness to maintain alignment. The actuator layers have an initial offset of $\Delta Z_0 = 310\,\mu m$ to prevent operation near $\Delta Z = 50\,\mu m$, where repulsive force markedly decreases (see Fig. 5).

### 5.2.1. Experimental

The actuator bottom layer is laminated onto a glass slide and secured to a 1-DoF rotational stage (Newport, MT-RS Series). The actuator top layer is suspended from a 3D-printed mount (Form-Labs, Form 2) on a 3-DoF linear stage (Newport, M-461 Series) to align the top layer over the bottom layer. The spring suspension (Fig. A.4) consists of four sets of cantilevered beams – compliant in $Z$, stiff in $X$/$Y$ – laser-cut from PET film (American Durafilm, 25 μm) as a single unit and adhered to the top layer with thermal adhesive. Two fiberoptic optical sensors – developed by E. Steltz [42] – provide displacement measurements of the actuator's top layer, and distinguish between $Z$-axis translational and $X$-axis rotational or flexing modes. The sensors are mounted parallel to one another in a 3D-printed clamp on an independent 3-DoF stage; sensor light is reflected off of matte paper sheets adhered onto the actuator top layer. The actuator is controlled from LabView, driven by a square-root of sinusoid signal supplied from the high-voltage amplifier, and monitored with voltage and current probes. The displacement is measured by the fiberoptic sensors and logged by the DAQ.

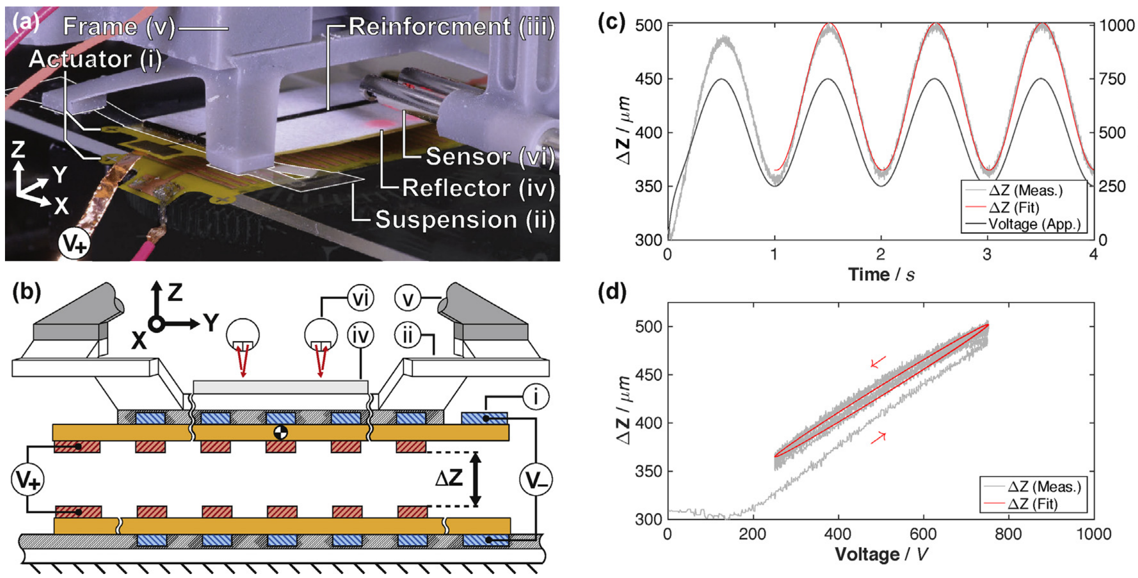


**Fig. 6.** Testing setup for free displacement characterization (a) with mechanical diagram (b) (electrical diagram in Fig. A.3). Of the two actuator layers (i), the bottom layer is bonded to a glass slide, and the top layer is reinforced with carbon fiber rods (iii) and connected to a 3D-printed frame (v) via a film cantilever spring suspension (ii, outlined in white). Displacement is monitored by optical emitter/detector sensors (vi) at two locations, reflected off a paper reflector (iv). Power is supplied by copper foil wires ($V_+/V_-$). (c and d) Displacement characterization with an applied sinusoid input voltage at 1 Hz/500 ± 250 V peak-to-peak. (c) Measured actuator $\Delta Z$ and actuator voltage versus time, with fit shown; (d) measured actuator $\Delta Z$ versus actuator voltage, with fit shown.

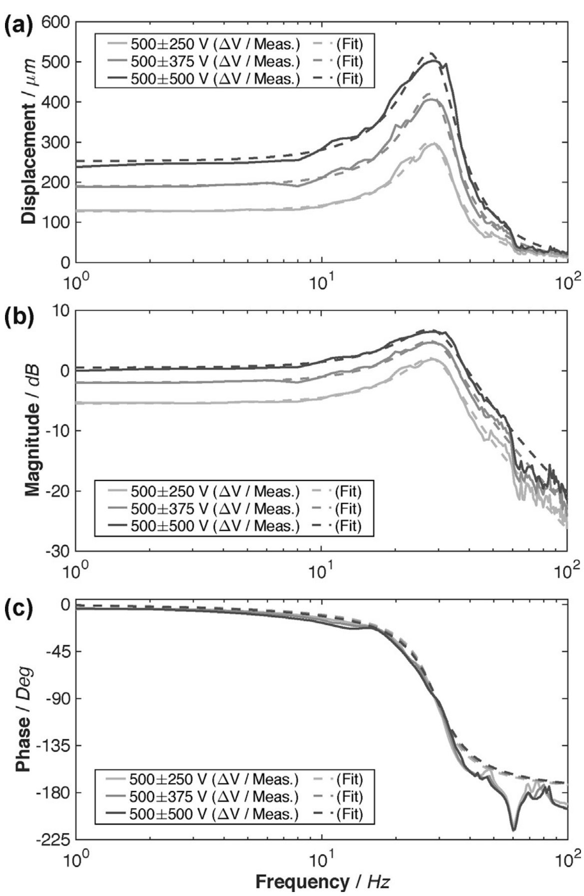


**Fig. 7.** Actuator displacement (peak-to-peak) (a), magnitude (b), and phase (c) versus frequency. Applied sinusoid input voltage at 1–100 Hz and 500 ± 250/375/500 V peak-to-peak. Data is fit with second-order linear systems. The actuator has stable 240–260 μm peak-to-peak displacements at sub-10 Hz frequencies, 511 μm displacements at 29 Hz resonance, and a 43 Hz open-loop bandwidth. The resonant peak has a quality factor of 1.59 (−3 dB from peak at 17.3 and 35.5 Hz).

For testing at different pressures, the full testing set-up is placed in a vacuum chamber (Abbess Instruments) and pumped down to the desired pressure using a vacuum pump (Pittsburgh Automotive, Two Stage Vacuum Pump). Vacuum feedthroughs for electricity and fiber-optic cables are used to drive the actuator and measure displacements.

### 5.2.2. Results

The actuator's measured displacement at low-frequency operation is shown in Fig. 6. A sinusoidal voltage (500 V bias and ±250 V amplitude) is applied to generate sinusoidal displacements of 132 μm peak-to-peak, after initial transients subside. Applying 500 ± 500 V generates larger 242 μm peak-to-peak displacements (Fig. A.5), at the cost of increased non-linear behavior and hysteresis – likely caused by viscoelastic behavior in the PET suspension or residual charge in the polyimide substrate.

The actuator's frequency-dependent displacement, magnitude, and phase behavior is shown in Fig. 7, and exhibits second-order behavior as modeled in Fig. A.6. Displacement is measured peak-to-peak during stable operation after transients subside. The actuator has a −3 dB bandwidth of 43 Hz. A stable $Z$-axis resonant mode at $f_0 = 29$ Hz has a peak displacement of $\Delta Z_{f_0} = 511$ μm and quality factor of $Q = 1.59$ (17.3–35.5 Hz). From the resonant behavior:

$$Q = \omega_0/\Delta\omega \tag{11}$$

$$\omega_0 = \sqrt{(k_A + k_S)/m_A} \tag{12}$$

$$b_S = (m_A\omega_0)/Q \tag{13}$$

Given the measured mass ($m_A = 135$ mg) and suspension stiffness ($k_S = 2.28$ N/m), the calculated net stiffness is 4.5 N/m ($k_A + k_S$) and the parallel effective electrostatic spring stiffness is 2.2 N/m ($k_A$). This agrees with the direct estimation of $k_A$ from Fig. 5a:

$$k_A = dF/dZ \approx \Delta F/\Delta Z = 2.36\ \text{N/m} \tag{14}$$

around the average operating point of $\Delta Z = 425$ μm and 500 V; the effect of $k_S$ is also plotted in Fig. 5a. Damping ($b_S = 0.0155$ Ns/m) is generated predominantly by the structure as opposed to air, as seen in Fig. A.7. $X$-axis rotational modes are predicted at 0.34 Hz and 5.8 kHz, and an $X$-axis bending mode predicted at 51 Hz is

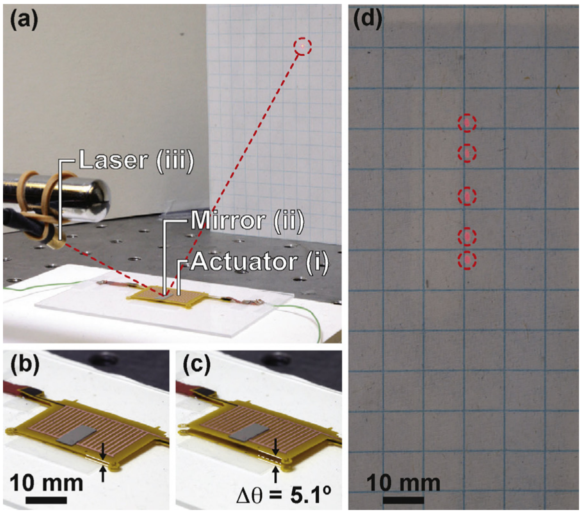


**Fig. 8.** (a) 1-DoF micro-mirror composed of a 2-layer RFA (i) and a metallized glass coverslip mirror (ii) controllably steers a laser beam (iii). Resonant performance at 16 Hz and 1000 V peak-to-peak, with: (b and c) actuation of RFA and (d) movement of laser dot at resonance (approx. 5.1°).

increased to above 200 Hz with stiffeners (reflectors and the carbon fiber reinforcing rods).

### 5.3. Internal power measurements

Mechanical power is calculated from the actuator's resonant behavior. Assuming a second-order system:

$$P = \frac{F^2}{2b_S}, \quad \text{with}\, F = (k_S + k_A) \cdot \Delta Z_{f_{DC}} \tag{15}$$

$\Delta Z$ at $f_{DC}$ = 1 Hz is provided in Fig. 7; the stiffnesses ($k_A$, $k_S$) and damping ($b_S$) are provided in Fig. A.6. Calculated mechanical power for the actuator at resonance is 38.0 μW.

Electrical power is calculated directly from the voltage and current probe measurements. The actuator behaves electrically as a non-ideal capacitor (Fig. A.8) – with parallel capacitance ($C$ = 840 pF), leak resistance ($R_C$ = 350 GΩ), and equivalent resistance ($R_{Eq}$ = 3.5 GΩ, at resonance) due to mechanical work – and is modeled in Fig. A.6. Electrical input power increases quadratically (1.78 mW at 1 Hz to 52.3 mW at 29 Hz resonance) and current increases linearly (2.73 μA to 75.5 μA) with frequency (Fig. A.9), using a 500 ± 500 V sinusoidal driving voltage.

The actuator has an electromechanical coupling factor of 1.8% (1 Hz) – 3.7% (29 Hz), based on:

$$\kappa = \sqrt{\frac{W_{Mech.}}{W_{Ele.}}} = \sqrt{\frac{(k_A + k_S)\Delta Z^2}{C\Delta V^2}} \tag{16}$$

The low coupling factor results from the actuator's large parallel plate capacitance between oppositely-charged electrodes in the V2 design.

## 6. Application example

We demonstrate a low-cost, 1-DOF micro-mirror driven by a flexible actuator for beam-steering applications (Fig. 8), such as laser mapping (on mobile robots) and laser engraving/marking. The micro-mirror system is self-contained (no extra transmission required), compact (45 × 15 mm, with 20 × 10 mm of active actuator area), and lightweight (290 mg, including a 14 mg/3 × 6 mm mirror). Its performance is demonstrated in the Supplemental Video.

The micro-mirror system consists of a 2-layer rotational RFA: the electrodes are fabricated from a single sheet of Pyralux AP that is folded in half to form the two layers. The bottom layer is adhered to a glass slide; the top layer is aligned/suspended by two polyimide torsional springs. The two layers are connected at the spring anchors, and share common $V_+/V_-$ terminals at these locations. Power to the top layer is supplied by copper traces on the spring suspension. The mirror is a metallized glass coverslip (100 μm thick), cut to size and placed on the top layer. The mirror reflects the beam from a laser diode mounted over the micro-mirror system.

The micro-mirror operates stably with open-loop control: applied voltages of 0–1000 V generate angular displacements of 2.2° (at low-frequencies) up to 5.1° (at 16 Hz resonance). The micro-mirror has peak input power of 2.57–41.0 mW and current of 3.81–60.4 μA at 1–16 Hz, respectively. Further, as the actuator displacement is proportional to its applied voltage, the micro-mirror can deflect controllably to any intermediate angles, unlike many commercial two-state (on/off) micro-mirrors.

Future applications of this actuator technology could also include large-area actuators (changing reflectivity/transparency for building thermal regulation [43]) and actuation on robot platforms that already employ high-voltage electrostatic grippers/adhesives [44].

## 7. Conclusion

In this paper, we have demonstrated meso-scale repulsive force electrostatic actuators that employ a redesigned electrode geometry and are made using a flex-circuit planar manufacturing process. The electrode design changes enable actuators that operate at 20 times greater field strength and generate 8.6–10.5× greater electrostatic pressure (over previous RFA electrode designs) at the same operating voltage and electrode feature size. At the same time, our actuators are extremely robust – individual actuators have been tested without failure for >700,000 cycles (see Note B.1) at up to 1000 V, 0.1–100 Hz, and 0.25–1.00 atm – since electrode defects or layer misalignment during operation reduce the repulsive force rather than causing a destructive shorting failure. This actuator design has other notable advantages:

- Stable operation with no pull-in behavior (unlike attractive force electrostatic actuators)
- Peak force generated at rest configuration (unlike attractive force electrostatic actuators)
- Voltage-controlled force and displacement, with no measured maximum $\Delta Z$ at which repulsive force becomes attractive (unlike prior RFA designs)
- Low mechanical hysteresis (unlike piezoelectric actuators and DEAs)
- Simple suspension for moving layers, since only one axis requires high stiffness and precise alignment
- No shorting failures if electrodes have manufacturing defects or if actuator layers are misaligned or touch, since oppositely-polarized electrodes are insulated by a resilient, incompressible dielectric substrate instead of air gaps (unlike prior RFA designs)

The fabrication process is comparable to conventional flexible PCB manufacturing processes, so cm-scale actuators can be immediately and inexpensively mass-produced. PCB vendors can even use the same Pyralux substrates we employ in this research to produce one- or two-sided actuator layers with higher density traces – 100 μm traces or gaps, compared to the 500 μm traces tested in-lab.

Fabricated actuators were observed to generate maximum repulsive forces up to 9.03 mN (36.1 Pa) and displacements of

242–511 μm across an open-loop stable bandwidth of 43 Hz with a 29 Hz resonant peak. A 290 mg micro-mirror system driven by an RFA was demonstrated to produce 5.1° rotations at 16 Hz resonance, and controllably steer a laser beam. Future work will investigate optimization of the actuator electrode geometry (for greater work output) and integrated capacitive sensing of actuator layer positions (for closed-loop control and drift compensation).

## Funding

Funding was provided by the National Science Foundation via Grant CMMI-1427096 and the Graduate Research Fellowship Program.

## Conflicts of interest

None.

## Acknowledgements

We thank K. Pister for advice on MEMS actuators; D. Steigmann for advice on finite differences modeling; H. Ota and K. Chen for mirror preparation; E. Steltz for characterization hardware; J. Yim for advice on simulations.

## Appendix A. Supplementary data

Supplementary data associated with this article can be found, in the online version, at https://doi.org/10.1016/j.sna.2017.12.054.

## References

[1] K. Pister, M. Judy, S. Burgett, R. Fearing, Microfabricated hinges, Sens. Actuators A: Phys. 33 (3) (1992) 249.
[2] A.M. Hoover, R.S. Fearing, Fast scale prototyping for folded millirobots, IEEE ICRA (2008) 886.
[3] D.W. Haldane, C. Casarez, J. Karras, J. Lee, C. Li, A. Pullin, E. Schaler, D. Yun, A. Javey, R.S. Fearing, Integrated manufacture of exoskeleton and sensing for folded millirobots, J. Mech. Robot. 7 (2) (2015) 19.
[4] R.J. Wood, S. Avadhanula, R. Sahai, E. Steltz, R.S. Fearing, Microrobot design using fiber reinforced composites, J. Mech. Des. 130 (5) (2008) 052304.
[5] J.P. Whitney, P.S. Sreetharan, K.Y. Ma, R.J. Wood, Pop-up book MEMS, J. Micromech. Microeng. 21 (11) (2011) 115021.
[6] T. Takahashi, K. Takei, A.G. Gillies, R.S. Fearing, A. Javey, Carbon nanotube active-matrix backplanes for conformal electronics and sensors, Nano Lett. 11 (12) (2011) 5408.
[7] M.T. Tolley, S.M. Felton, S. Miyashita, D. Aukes, D. Rus, R.J. Wood, Self-folding origami: shape memory composites activated by uniform heating, Smart Mater. Struct. 23 (9) (2014) 094006.
[8] M.M. Hamedi, V.E. Campbell, P. Rothemund, F. Güder, D.C. Christodouleas, J.-F. Bloch, G.M. Whitesides, Electrically activated paper actuators, Adv. Funct. Mater. 26 (15) (2016) 2446–2453.
[9] N.T. Jafferis, M. Lok, N. Winey, G.-Y. Wei, R.J. Wood, Multilayer laminated piezoelectric bending actuators: design and manufacturing for optimum power density and efficiency, Smart Mater. Struct. 25 (5) (2016) 055033.
[10] J. Shintake, S. Rosset, B. Schubert, D. Floreano, H. Shea, Versatile soft grippers with intrinsic electroadhesion based on multifunctional polymer actuators, Adv. Mater. 28 (2) (2016) 231–238.
[11] S. Shian, K. Bertoldi, D.R. Clarke, Dielectric elastomer based “grippers” for soft robotics, Adv. Mater. 27 (43) (2015) 6814.
[12] K. Minami, S. Kawamura, M. Esashi, Fabrication of distributed electrostatic micro actuator (DEMA), J. Microelectromech. Syst. 2 (3) (1993) 121–127.
[13] M. Ito, K. Saneyoshi, Development of large-scale stacked-type electrostatic actuators for use as artificial muscles, Adv. Robot. 1864 (March) (2014) 1–9.
[14] A.S. Chen, H. Zhu, Y. Li, L. Hu, S. Bergbreiter, A paper-based electrostatic zipper actuator for printable robots, IEEE ICRA (2014) 5038.
[15] H. Shigemune, S. Maeda, V. Cacucciolo, Y. Iwata, E. Iwase, S. Hashimoto, S. Sugano, Printed paper robot driven by electrostatic actuator, IEEE Robot. Autom. Lett. 2 (2) (2017) 1001.
[16] I. Hunter, S. Lafontaine, A comparison of muscle with artificial actuators, in: IEEE Solid-State Sens. Actuators, 1992, pp. 178–185.
[17] M. Karpelson, R.J. Wood, A review of actuation and power electronics options for flapping-wing robotic insects, IEEE ICRA (2008) 779–786.
[18] S. He, R. Ben Mrad, J. Chong, Repulsive-force out-of-plane large stroke translation micro electrostatic actuator, J. Micromech. Microeng. 21 (7) (2011) 075002.
[19] S. He, R. Ben Mrad, Large-stroke microelectrostatic actuators for vertical translation of micromirrors used in adaptive optics, IEEE Trans. Ind. Electron. 52 (4) (2005) 974–983.
[20] K. Meijer, M.S. Rosenthal, R.J. Full, Muscle-like actuators? A comparison between three electroactive polymers, Proc. SPIE 4329 (2001) 7.
[21] I. Penskiy, S. Bergbreiter, Optimized electrostatic inchworm motors using a flexible driving arm, J. Micromech. Microeng. 23 (1) (2013) 015018.
[22] S.H. Goodwin-Johansson, S.M. Bobbio, C. Bartlett, N. Eleyan, J. Jacobson, J.E. Mancusi, L. Yadon, C. Ball, T.D. DuBois, W.D. Palmer, D.G. Vellenga, F.M. Tranjan, Measured forces and displacements of integrated force arrays, Proc. SPIE 2642 (1995) 52.
[23] T. Niino, S. Egawa, T. Higuchi, High-power and high-efficiency electrostatic actuator, in: Proc. of IEEE MEMS, IEEE, 1993, pp. 236–241.
[24] E. Husain, R.S. Nema, Analysis of Paschen curves for Air, N2, and SF6 using the Townsend breakdown equation, IEEE Trans. Electr. Insul. EI-17 (4) (1982) 350–353.
[25] P. Slade, E. Taylor, Electrical breakdown in atmospheric air between closely spaced (0.2 μm–40 μm) electrical contacts, IEEE Trans. Comp. Pack. Tech. 25 (3) (2002) 390–396.
[26] DuPont, DuPont® Kapton®, Tech. Rep., 2012.
[27] DuPont, DuPont Pyralux AP, Tech. Rep., 2016.
[28] R. Yeh, S. Hollar, K. Pister, Single mask, large force, and large displacement electrostatic linear inchworm motors, J. Microelectromech. Syst. 11 (4) (2002) 330–336.
[29] W.C. Tang, T.-C. Nguyen, R. Howe, Laterally driven polysilicon resonant microstructures, IEEE MEMS, vol. 20 (1989) 53–59.
[30] S. Bobbio, M. Kellam, B. Dudley, S. Goodwin-Johansson, S. Jones, J. Jacobson, F. Tranjan, T. DuBois, Integrated force arrays, IEEE MEMS (1993) 149.
[31] R.E. Pelrine, R.D. Kornbluh, J.P. Joseph, Electrostriction of polymer dielectrics with compliant electrodes as a means of actuation, Sens. Actuators A: Phys. 64 (1) (1998) 77–85.
[32] R. Pelrine, R. Kornbluh, Q. Pei, J. Joseph, High-speed electrically actuated elastomers with strain greater than 100%, Science 287 (5454) (2000) 836–839.
[33] H. Wang, A. Yamamoto, T. Higuchi, Electrostatic-motor-driven electroadhesive robot, IEEE/RSJ IROS (2012) 914;
W.C. Tang, Electrostatic comb drive for resonant sensor and actuator applications (Ph.D. thesis), University of California, Berkeley, 1990.
[34] W.C. Tang, M.G. Lim, R.T. Howe, Electrostatic comb drive levitation and control method, J. Microelectromech. Syst. 1 (4) (1992) 170–178.
[35] S. He, R. Ben Mrad, Performance assessment of a multi-level repulsive-force out-of-plane microelectrostatic actuator, Can. J. Electr. Comput. Eng. 31 (2) (2006) 71–75.
[36] S. He, R. Ben Mrad, Design, modeling, and demonstration of a MEMS repulsive-force out-of-plane electrostatic micro actuator, J. Microelectromech. Syst. 17 (3) (2008) 532–547.
[37] S. He, R. Ben Mrad, J.S. Chang, Development of a high-performance microelectrostatic repulsive-force rotation actuator, J. Microelectromech. Syst. 19 (3) (2010) 561–569.
[38] S. Towfighian, S. He, R. Ben Mrad, A low voltage electrostatic micro actuator for large out-of-plane displacement, ASME IDETC/CIE (2014) 1–7.
[39] J. Batterson, Second Order Finite Difference Schemes for non-Uniform Grid Spacing, Auburn University, 2014, pp. 10.
[40] T. Lebey, P. Castelan, G. Montanari, I. Ghinello, Influence of PWM-type voltage waveforms on reliability of machine insulation system, IEEE ICHQP, vol. 2 (1998) 994–998.
[41] D. Fabiani, G.C. Montanari, A. Cavallini, G. Mazzanti, Relation between space charge accumulation and partial discharge activity in enameled wires under PWM-like voltage waveforms, IEEE Trans. Dielectr. Electr. Insul. 11 (3) (2004) 393–405.
[42] E. Steltz, Optical Position Sensing for Characterization of the Micromechanical Flying Insect (M.s. thesis), University of California, Berkeley, 2006.
[43] X. Zhang, Z. Yu, C. Wang, D. Zarrouk, J.-W.T. Seo, J.C. Cheng, A.D. Buchan, K. Takei, Y. Zhao, J.W. Ager, J. Zhang, M. Hettick, M.C. Hersam, A.P. Pisano, R.S. Fearing, A. Javey, Photoactuators and motors based on carbon nanotubes with selective chirality distributions, Nat. Commun. 5 (2014) 1–8.
[44] E. Schaler, D. Ruffatto III, P. Glick, V. White, A. Parness, An electrostatic gripper for flexible objects, IEEE IROS (2017) 1172–1179.

## Biographies

**Ethan W. Schaler** received the B.S. degree in Mechanical Engineering from the University of Maryland, College Park, in 2011, and the M.Phil. degree in Micro and Nanotechnology Enterprise from the University of Cambridge in 2012. He is currently working towards the Ph.D. degree in the Department of Electrical Engineering and Computer Sciences, University of California, Berkeley.

His research interests include the design, modeling, fabrication, and control of flexible electrostatic actuators, adhesives, and sensors, especially as they apply to milli-robotics.

**Tarek I. Zohdi** received the B.S. and M.S. degrees in Mechanical Engineering from Louisiana State University in 1989 and 1991, respectively, the Ph.D. degree in Computational and Applied Math from the University of Texas, Austin, in 1997, and the Habilitation in Mechanics from Gottfried Wilhelm Leibniz Universities Hannover in 2002. In July 2012, he was appointed Chair of the Designated Emphasis

Program in Computational and Data Science and Engineering (DE-CSE) at UC Berkeley. Previously, he has served as Chair of the Engineering Science Program at UC Berkeley (2008–2012) and Vice-Chair for Instruction in the Department of Mechanical Engineering (2009–2012). He is currently a Chancellors Professor of Mechanical Engineering and holder of the W. C. Hall Family Endowed Chair in Engineering. He also holds a Staff Scientist position at Lawrence Berkeley National Labs and an Adjunct Scientist position at the Children's Hospital Oakland Research Institute.

His research interests include in micromechanical material design, particulate flow and the mechanics of high-strength fabric, with emphasis on computational approaches for advanced manufacturing and nonconvex multiscale-multiphysics inverse problems, in particular addressing the important issue of how large numbers of micro-constituents interact to produce macroscale aggregate behavior.

**Ronald S. Fearing** received the S.B. and S.M. degrees in Electrical Engineering and Computer Sciences from the Massachusetts Institute of Technology in 1983, and the Ph.D. degree in Electrical Engineering from Stanford University in 1987. He is a professor in the Dept. of Electrical Engineering and Computer Sciences at Univ. of California, Berkeley, which he joined in Jan. 1988. He was Vice-Chair for Undergraduate Matters from 2000–2006, and is Vice-Chair for Graduate Matters (2016–present). He received the Presidential Young Investigator Award in 1991, and is the co-inventor on 18 US and international patents.

His current research interests are in bioinspired milli-robotics, including flying and crawling milli-robots, cooperative locomotion, rapid prototyping, parallel nano-grasping (gecko adhesion) and micro-assembly. He has worked in tactile sensing, teletaction, and dexterous manipulation.